

Plasmon-Enhanced Multiphoton Polymer Crosslinking for Selective Modification of Plasmonic Hotspots

Yevhenii M. Morozov,* Nestor Gisbert Quilis, Stefan Fossati, Laura De Laporte, Claudia Gusenbauer, Andreas Weber, Jose Luis Toca-Herrera, Fiona Wiesner, Ulrich Jonas, and Jakub Dostalek*



Cite This: *J. Phys. Chem. C* 2024, 128, 18641–18650



Read Online

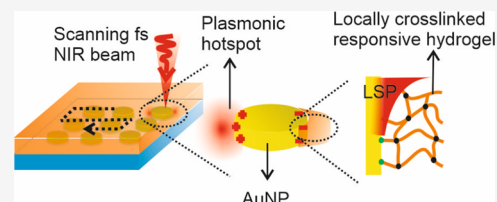
ACCESS |

 Metrics & More

 Article Recommendations

 Supporting Information

ABSTRACT: A novel approach to selectively modify narrow subareas of metallic nanostructures adjacent to plasmonic hotspots, where strong electromagnetic field amplification occurs upon localized surface plasmon (LSP) excitation, is reported. In contrast to surface plasmon-triggered polymerization, it relies on plasmonically enhanced multiphoton crosslinking (MPC) of polymer chains carrying photoactive moieties. When they are contacted with metallic nanostructures and irradiated with a femtosecond near-infrared beam resonantly coupled with LSPs, the enhanced field intensity locally exceeds the threshold and initiates MPC only at plasmonic hotspots. This concept is demonstrated by using gold nanoparticle arrays coated with two specifically designed polymers. Local MPC of a poly(*N,N*-dimethylacrylamide)-based copolymer with an anthraquinone crosslinker is shown via atomic force microscopy. Additionally, MPC is tested with a thermoresponsive poly(*N*-isopropylacrylamide)-based terpolymer. The reversible thermally induced collapse and swelling of the MPC-formed hydrogel at specific nanoparticle locations are confirmed by polarization-resolved localized surface plasmon resonance (LSPR) spectroscopy. These hybrid metallic/hydrogel materials can be further postmodified, offering attractive characteristics for future spectroscopic/bioanalytical applications.



INTRODUCTION

Optical nanoantennas that allow for nanoscale confinement of the electromagnetic field play a pivotal role in numerous important research fields and application domains relying on optical spectroscopy and photochemical reactions in tightly confined volumes.^{1–5} For example, such nanoantennas have enabled the study of fundamental optical phenomena at the single emitter level (such as organic fluorophore molecules, quantum dots, or nitrogen-vacancy centers in diamonds),^{6–9} in single biomolecule interaction analysis by using labeling with such fluorescent species,¹⁰ or on hot electron-facilitated catalysis.^{11,12} Metallic nanostructures and nanoparticles (NPs) represent key building blocks for the construction of optical nanoantennas. The resonant excitation of localized plasmons (LSPs) on such metallic NPs allows for deep subwavelength confinement of light energy due to collective oscillations of electron density and the associated electromagnetic field.^{13,14} The optical excitation of LSPs is accompanied by a strong enhancement of the incident light intensity, which is not homogeneously distributed around metallic NPs but occurs at specific spatially distinct regions (e.g., edges/tips or gaps between closely arranged metallic objects) that are commonly referred to as “plasmonic hotspots”.¹⁵ Therefore, various strategies to spatially control the attachment of functional chemical moieties at these regions have been pursued for precise control and to maximize the efficiency of their interaction with LSPs.^{15–18} These include the use of photoresist mask windows made by electron beam

lithography to overlay with plasmonic hotspots,¹⁹ development of orthogonal surface chemistries,^{16,20} and employment of a static electric field gradient for attracting the species at sharp parts of metallic nanostructures.²¹ The use of chemical reactions that are locally triggered by LSPs has been explored based on the LSP-generated hot electrons,²² two-photon polymerization,²³ and by using multiphoton absorption-activated linkers for docking of proteins^{24–26} and local photocrosslinking of protein hydrogel.²⁷ In addition, LSP-induced polymerization has been shown to allow for local attachment of nanoscale photoresist features overlapping with plasmonic hotspots^{28–32} and later it was intensively used for the preparation of hybrid polymer/metal materials and probing of local chemical reactions.^{33–37}

Multiphoton absorption photochemistry has become particularly important in mask-less lithography^{38,39} developed for the preparation of complex structures with a spatial resolution down to a hundred nanometers.⁴⁰ Up to now, multiphoton lithography techniques have been utilized for the fabrication of objects with a well-controlled three-dimensional geometry serving in diverse areas including micro-optics,^{41–43} micro-

Received: September 2, 2024

Revised: October 7, 2024

Accepted: October 11, 2024

Published: October 22, 2024



robotics,^{44,45} tissue engineering,^{46–50} and drug delivery⁵¹ to mention a few examples. The vast majority of materials that are structured with the help of multiphoton absorption lithography rely on a polymerization process.⁵² Typically, a femtosecond (fs) pulsed laser beam with a near-infrared (NIR) wavelength is focused and scanned through a liquid monomer to initiate polymerization in a small focal volume, where the threshold for initiation is exceeded.⁵³ Only along the path of the NIR beam are the included photoinitiator molecules excited by the sequential absorption of photons to initiate a free-radical polymerization reaction locally solidifying the liquid photoresist. Besides multiphoton lithography relying on a polymerization mechanism, a recently reported alternative is based on multiphoton crosslinking (MPC) of soluble polymers employed as solid thin films.⁵⁴ Their polymer backbones contain photoactive moieties that were excited by a scanned focused NIR beam to induce MPC, resulting in thermoresponsive biofunctional hydrogels when a postmodification step is utilized.⁵⁵ The MPC process was investigated in dependence on the type of crosslinker and its means of conjugation to the polymer backbone.⁵⁵ This crosslinking-based approach, in contrast to the more frequently used polymerization, allows for the creation of structures from a compact dry polymer layer, eliminating the risk of residual monomer and/or photoinitiator leakage during swelling and offering the advantage of higher chemical precision when incorporating multiple functionalities during the polymer presynthesis stage.

In the present work, we report on a new generic approach to chemically modify narrow zones of metallic nanostructures, where plasmonic hotspots occur. The strategy employs polymer chains with incorporated photoactive crosslinkers that can be triggered by the multiphoton absorption process for their simultaneous attachment and crosslinking at the plasmonic hotspot where the MPC threshold is locally reached. To the best of our knowledge, in contrast to the plasmonically driven polymerization, this type of plasmonically mediated photochemistry—plasmon-enhanced multiphoton crosslinking (PE-MPC)—has not yet been reported, despite its potential for preparing well-controlled hybrid metal/hydrogel nanomaterials. This method leverages the already established multiphoton lithography tools and offers the capability for selective local postmodification of the resulting structures. The reliability of the approach is demonstrated by using two types of polymers that form locally attached hydrogel nanostructures at plasmonic hotspots after swelling in aqueous media. The successful preparation of such materials is documented for optimized writing conditions by atomic force microscopy (AFM) measurements of the local topography and Young's modulus and by characterizing the nanoscopic domains of the thermoresponsive hydrogel matrix with polarization-resolved localized surface plasmon resonance (LSPR) measurements.

MATERIALS AND METHODS

Materials. Poly(DMAA-*co*-AAHAQ) was synthesized as previously reported.⁵⁴ Poly(NIPAAm-*co*-MAA-*co*-BPQAAM) was synthesized as previously reported.⁵⁵ Benzophenone disulfide (BPDiS) was synthesized as reported elsewhere.⁵⁶ S1805 resist and AZ303 developer were purchased from Micro Resist Technology GmbH (Germany). Dimethyl sulfoxide (DMSO) was purchased from Sigma-Aldrich, Austria.

Preparation of Hydrogel-Coated Gold Particle Arrays. Periodic arrays of gold nanoparticles (AuNPs) with a diameter

$D = 185 \pm 10$ nm and period $\Lambda = 400$ nm (in the case of structures with poly[DMAA-*co*-AAHAQ]) and with a diameter $D = 165 \pm 10$ nm and period $\Lambda = 400$ nm (in the case of structures with poly[NIPAAm-*co*-MAA-*co*-BPQAAM] terpolymer) were employed as plasmonic substrates. Briefly, a BK7 glass slide was coated with a 2 nm thick chromium layer and 50 nm thick gold layer by thermal evaporation (UNIVEX 450, Helmut Heller GmbH, Germany). Then, an S1805 positive photoresist (1:2 ratio diluted with propylene glycol monomethyl ether acetate) was spun on the gold surface, yielding a layer with a thickness of 120 nm. A periodic interference pattern was recorded into the photoresist layer by employing a He–Cd laser ($\lambda = 325$ nm) with Lloyd's mirror setup as previously reported by our group.⁵⁷ The well-defined resist particles with subwavelength dimensions were etched by using the AZ-303 developer (1:15 ratio with deionized water). Finally, the inscribed pattern was transferred to the gold film by using dry etching with an argon milling system (IonSys 500, Roth&Rau, Germany). The remaining photoresist was removed by applying an oxygen plasma treatment. The prepared plasmonic substrate was immersed overnight in a 1 mM solution made of BPDiS dissolved in DMSO in order to form a self-assembled monolayer on the pristine gold surface. The photocrosslinkable polymer thin film was subsequently spun (from ethanolic solution with 3 and 2% w/w of poly(DMAA-*co*-AAHAQ) and poly(NIPAAm-*co*-MAA-*co*-BPQAAM), respectively) on top of the AuNP arrays at a rate of 2000 rpm for 60 s and dried overnight in a vacuum oven at $T = 50$ °C.

Plasmon-Enhanced Multiphoton Crosslinking of Poly(DMAA-*co*-AAHAQ). Poly(DMAA-*co*-AAHAQ) was deposited on the top of AuNP arrays carried by a glass substrate, as described above. The substrate was mounted into the Photonic Professional (GT) system from Nanoscribe GmbH for the recording step (with a wavelength of the emitted light centered at 780 nm),⁵⁸ with the surface carrying the plasmonic architectures facing a clean coverslip. The interface was selected by focusing on the surface with the gold nanoparticle arrays, and the correct z plane was set by recording square features with the highest writing speed and laser power P_L and visually observing the recording of the micrometer-size features with the equipped microscope camera. Once the proper interface was found, a recording script was loaded and squares ($100 \times 100 \mu\text{m}^2$) with different parameters were inscribed. The scan speed was varied between 10,000 and 2500 $\mu\text{m s}^{-1}$ and the laser power $P_L = 2–5$ mW. After the recording step, the unbound polymer was removed by rinsing with ethanol.

Plasmon-Enhanced Multiphoton Crosslinking of Poly(NIPAAm-*co*-MAA-*co*-BPQAAM). Poly(NIPAAm-*co*-MAA-*co*-BPQAAM) was deposited on the top of AuNP arrays carried by a glass substrate, as described above. The substrate was mounted into a home-built general-purpose multiphoton absorption lithography setup for the recording step (details of the setup can be found in refs 55,59). The wavelength of the emitted light of the home-built setup is centered at 785 nm. After the selection of the correct z plane, a rectangular area of $75 \times 50 \mu\text{m}^2$ was recorded. The laser power P_L was varied between 10 and 15 mW, and the dwelling time t_d was varied between 1 and 5 s.

Morphological Characterization. For topography measurements of the AuNP arrays with attached polymer networks, AFM height topography was acquired with the help of a Bruker's Dimension Icon (Bruker) instrument operated in

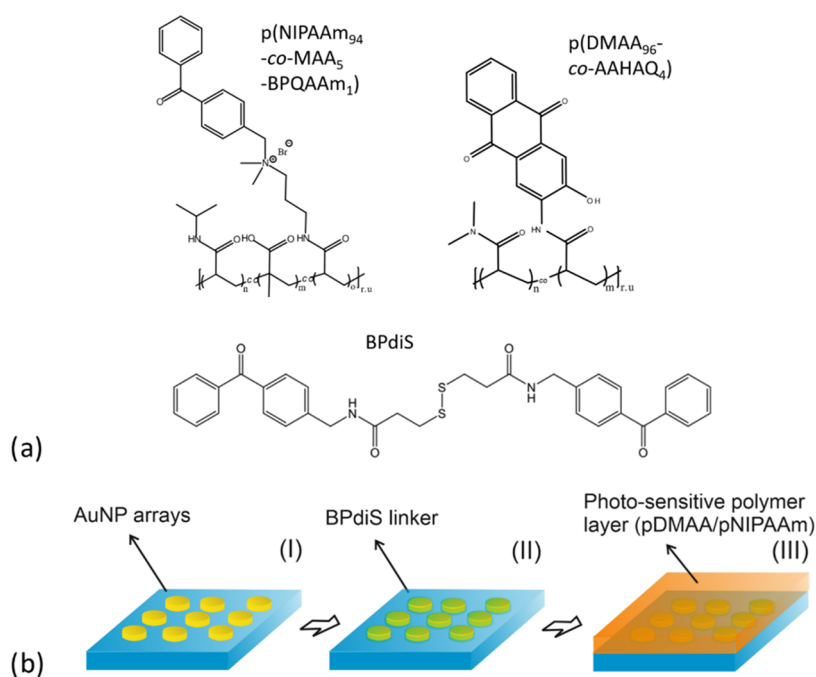


Figure 1. (a) Chemical structure of photocrosslinkable poly(DMAA₉₆-*co*-AAHAQ₄) and poly(NIPAAm₉₄-*co*-MAA₅-*co*-BPQAAm₁) polymers and BPdiS linker and (b) schematics of the preparation procedure for the Au nanoparticle arrays coated with photocrosslinkable polymers.

tapping mode. For all measurements, triangular silicon nitride SCANASYST-AIR cantilevers (Bruker) with a nominative spring constant k of 0.4 N/m, a resonance frequency of 70 kHz (in air), and a tip radius of 2 nm were used. Before each experiment, the true spring constant in air was determined via thermal tuning calibration after determining the deflection sensitivity. The AFM measurements in water were carried out with a Nanowizard (JPK III, Germany) instrument equipped with the inverse microscope and a liquid chamber. Imaging of the samples in water was performed in contact mode and quantitative imaging (QI) mode (0.3 N/m cantilevers with a 10 nm tip radius). The mapping to determine the mechanical properties was conducted in force volume mode both in water and in air (force curve at each pixel with 10 $\mu\text{m/s}$, maximum force of 5 nN, up to 200 \times 200 resolution for a 2 \times 2 μm image). Young's modulus was determined by fitting the approach section with the elastic model (Hertz model with Sneddon extension for geometry). Cantilever properties: $k = 9$ N/m (± 2), resonance frequency 150 kHz, beam shaped, 175 μm , Al coating on the backside, OPUS shape (tetrahedral), radius below 7 nm, 35° back angle.

Electromagnetic Simulations. The Ansys Lumerical FDTD numerical simulation package was used for all electromagnetic modeling. Geometrical parameters for arrays of AuNPs were used according to those mentioned in the main text and the [Supporting Information](#). Below the AuNPs, a chromium layer with a thickness of 2 nm was assumed. A dielectric medium with a refractive index of 1.5 (non-dispersive) representing the BK7 glass was used as a substrate. As a superstrate, a medium with a refractive index of 1.45 (nondispersive) representing the polymer in a dry state was used. A plane wave made normally incident at the structure was used as an excitation source. Periodic (along the x - and y -axes) and perfectly matched layer absorbing (at the z -axis, 1.2 μm above and below the structure) boundary conditions were

applied. Au and Cr optical properties were taken from the literature.^{60,61}

RESULTS AND DISCUSSION

Design of Polymers and Plasmonic Nanostructures.

The proposed concept was pursued with two types of photocrosslinkable polymers shown in [Figure 1a](#), which form a polymer network via MPC and subsequently a hydrogel after swelling with water. Details on the mechanism of the photoinitiated crosslinking mechanism was the subject of previous studies,^{54,55} and the copolymer poly(*N,N*-dimethylacrylamide-*co*-acylamido-3-hydroxyanthraquinone), abbreviated as poly(DMAA₉₆-*co*-AAHAQ₄), was chosen for the preparation of rigid hydrogel structures. It is ascribed to an apparently higher crosslink density due to a high ratio of anthraquinone-based photocrosslinking units (4% AAHAQ polymerization feed) in the polymer backbone. In addition, the terpolymer poly(NIPAAm₉₄-*co*-MAA₅-*co*-BPQAAm₁) was prepared by copolymerization of *N*-isopropylacrylamide (NIPAAm) with [(4-benzoylphenyl)methyl]dimethyl[3-(prop-2-enamido)-propyl]azanium bromide (BPQAAm) and methacrylic acid (MAA). This polymer carried low amounts of photocrosslinking units (1% BPQAAm in the polymerization feed) and allowed for the preparation of softer thermoresponsive hydrogel features. It was possible to modulate the degree of swelling for this pNIPAAm-based hydrogel with lower critical solution temperature (LCST) behavior by changing the temperature from below the volume phase transition temperature (VPTT), where the polymer network contacting water is in a swollen state, to above the VPTT, where it collapses. In further experiments, the polymers were crosslinked by using a focused beam of pulsed femtosecond (fs) lasers emitting at a wavelength of $\lambda_L = 780\text{--}785$ nm that was scanned over the substrate with a home-built setup^{55,59} and alternatively by a commercially available Photonic Professional (GT) system (Nanoscribe GmbH, Germany).⁵⁸

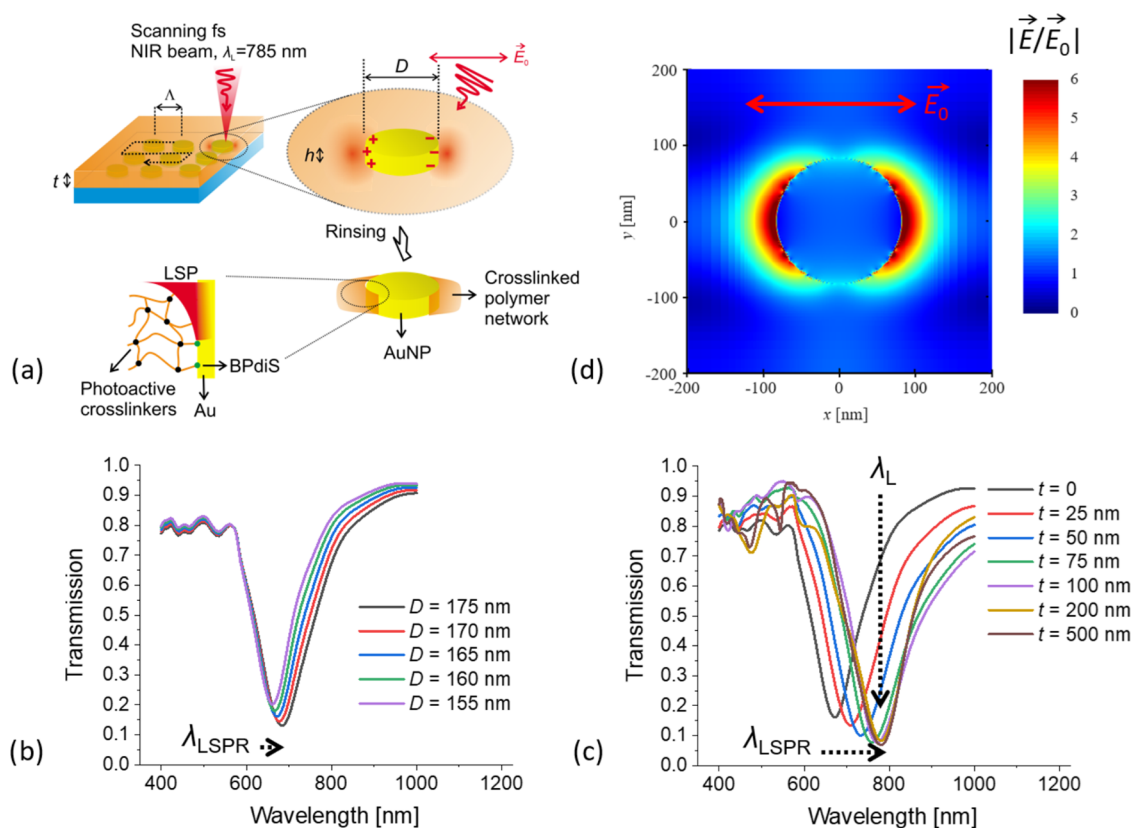


Figure 2. (a) Schematics of the crosslinking of polymer layer via PE-MPC. (b) Simulations of transmission spectra for AuNP arrays with varied Au disk diameters $D = 155$ – 175 nm and when the polymer overlayer is absent (thickness $t = 0$). (c) Simulated transmission spectra for $D = 165$ nm when the polymer overlayer thickness t is increased up to 500 nm. (d) Simulated near-field distribution of the electric field intensity amplitude upon resonant excitation of LSPs on AuNP with $D = 165$ nm at $\lambda_L = 785$ nm and $t = 100$ nm. In all simulations, the period of the AuNP arrays was $\Lambda = 400$ nm.

The overall preparation route of the substrates used in PE-MPC experiments is summarized in Figure 1b. Briefly, arrays of cylindrically shaped AuNPs were prepared by using UV laser interference lithography in combination with Ar ion milling (step I).⁵⁷ Afterward, the gold surface of AuNPs was reacted with 3,3'-disulfanediylbis(*N*-(4-benzoylbenzyl)propanamide) (BPDiS) to serve as a photoactive linker (step II). Finally, a photocrosslinkable polymer layer (pDMAA- or pNIPAAm-based) with a thickness t of about 100 nm was deposited over the AuNP arrays (step III) prior to MPC with a focused femtosecond NIR laser beam.

The MPC process of the polymer chains at plasmonic hotspots was induced by scanning a focused NIR femtosecond laser beam of a wavelength λ_L over the polymer-embedded AuNP arrays, as schematically presented in Figure 2a. The AuNPs are made resonant at a wavelength of λ_{LSPR} that is coincident with that of the NIR fs laser beam λ_L . For the optimum scanning speed and intensity of the NIR fs laser beam P_L , the resonant excitation of LSPs increases the electromagnetic field intensity above the threshold of the (nonlinear) multiphoton absorption process that activates crosslinker moieties (BPQAAm or AAHAQ) and allow for the formation of the surface-attached polymer network. The laser beam intensity P_L is chosen such that the NIR electromagnetic field intensity further away from the metallic nanostructure surface stays below the threshold. Therefore, any polymer chains outside the plasmonic hotspots are not crosslinked and upon rinsing with a solvent are washed away. This procedure and parameter optimization are described in our previous

work,⁵⁵ and it is also important to note that it is crucial to not exceed the threshold, above which the structure is damaged by increased temperature (see Figure S1, where certain laser power and writing speed values resulted in the structural burning of the poly[DMAA₉₆-co-AAHAQ₄] polymer).

The geometry, which enables matching of the LSPR wavelength λ_{LSPR} with that of NIR fs laser λ_L , was identified by using finite-difference time-domain (Ansys Lumerical FDTD) simulations. The optimum Au disk diameter D and thickness of the polymer overlayer t were determined for cylindrically shaped AuNPs with a height of $h = 50$ nm when arranged in arrays with a period of $\Lambda = 400$ nm. As can be seen in Figure 2b, the resonant excitation of LSPs manifests itself as a narrow absorption band in the transmission spectrum with its minimum corresponding to λ_{LSPR} . The resonant wavelength λ_{LSPR} shifts from 650 to 690 nm when increasing the AuNP diameter D from 155 to 175 nm in a structure without the polymer layer (thickness $t = 0$). Figure 2c shows that the presence of the polymer overlayer red-shifts the resonant wavelength λ_{LSPR} and for the AuNP diameter $D = 165$ and $t > 100$ nm, it yields $\lambda_{LSPR} = 780$ – 790 nm close to the laser wavelength λ_L . An additional set of FDTD simulations was run to simulate the near-field distribution of electric field intensity upon the resonant excitation of LSPs at $\lambda_L = \lambda_{LSPR} = 785$ nm for this geometry. The cross section presented in Figure 2d shows that the peak enhancement of the electric field intensity $|E|$ reaches ~ 6 with respect to the incident field E_0 . It exhibits a two-lobe distribution profile that is characteristic of a dipole LSP mode aligned in the direction

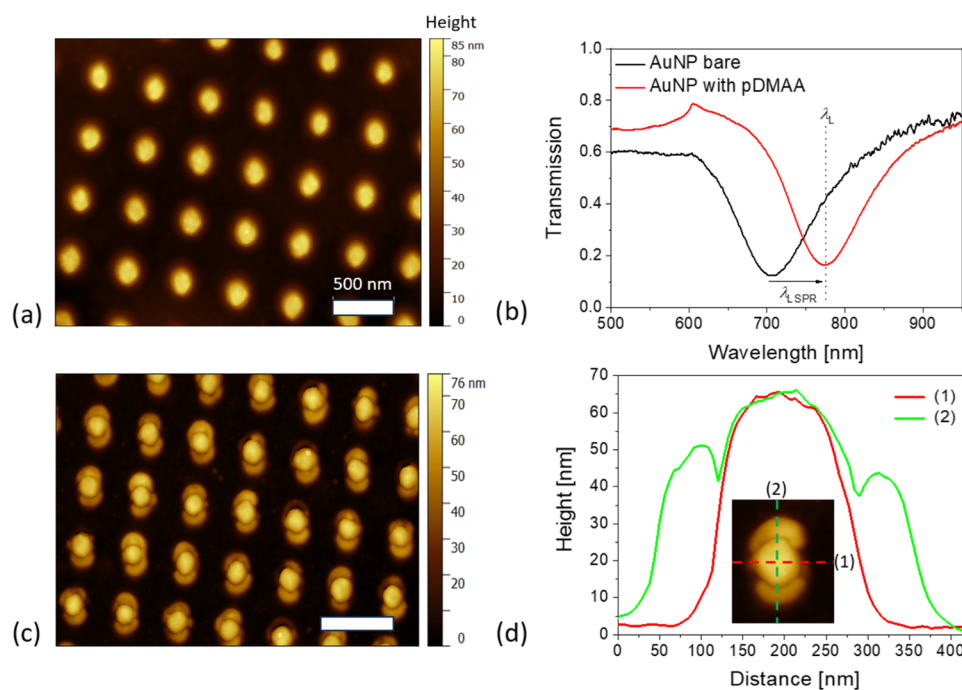


Figure 3. (a) AFM topography of the bare AuNP arrays and (b) measured LSPR transmission spectra before (black line) and after the coating (red line) with an uncrosslinked poly(DMAA_{96-co-AAHAQ}₄) layer of thickness $t = 154$ nm. (c) AFM height topography image of the same AuNP arrays after PE-MPC of poly(DMAA_{96-co-AAHAQ}₄) and rinsing. (d) Respective cross sections for individual AuNPs. All AFM measurements were performed in the air.

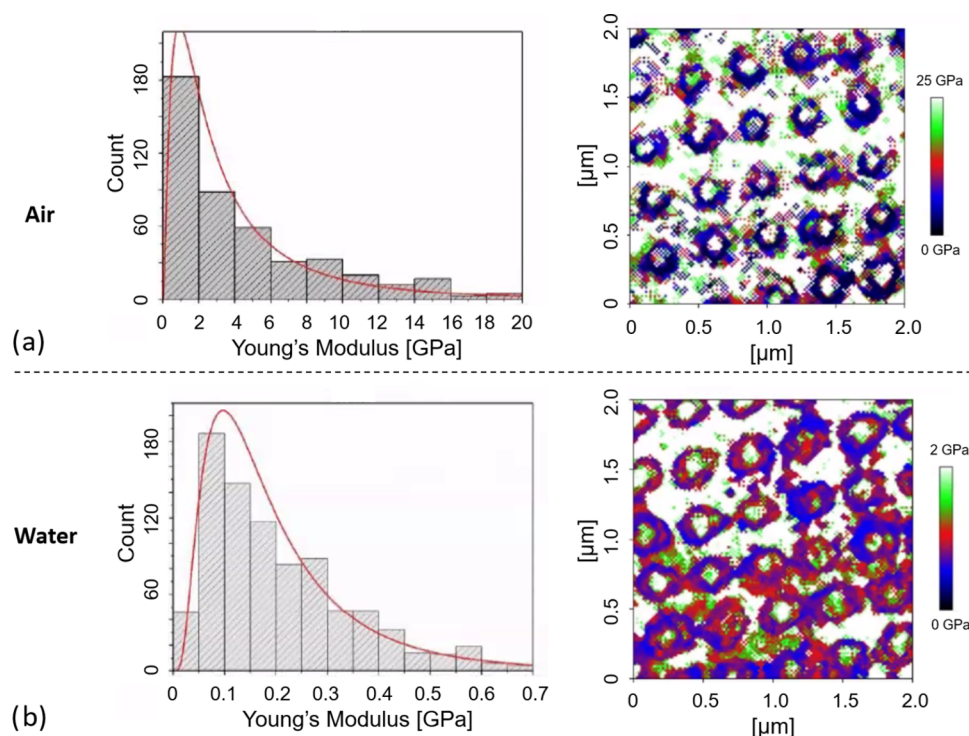


Figure 4. Comparison of Young's moduli for the AuNP–polymer network hybrid system in (a) air and (b) water, with histograms on the left-hand side displaying Young's moduli of 30 nanoparticles at random orientations and its corresponding logarithmic fitting.

of the incident field polarization. (A complete set of numerical results for the AuNP array with varying parameters can be found in Figure S2.)

Topography and Young's Modulus Measurements. AFM was first used for the observation of morphology and elasticity of the poly(DMAA_{96-co-AAHAQ}₄) polymer networks

attached to AuNP plasmonic hotspots. In this experiment, AuNP arrays with a diameter D of 185 ± 10 nm, a height of $h = 50$ nm, and a period of $\Lambda = 400$ nm were used with the respective height topography shown in Figure 3a. After depositing the poly(DMAA_{96-co-AAHAQ}₄) copolymer layer with a thickness of $t = 154$ nm (determined with the surface

plasmon resonance measurement; see Figure S3), the LSPR wavelength of the AuNP array was shifted from $\lambda_{\text{LSPR}} = 700$ to 780 nm as confirmed by optical transmission spectroscopy (see Figure 3b). This λ_{LSPR} value is close to λ_L of the NIR beam of the used multiphoton lithographer, and it agrees with the previous simulations. AuNP arrays coated with poly(DMAA₉₆-*co*-AAHAQ₄) overlayer were scanned “line-by-line” with a focused NIR fs laser beam using a power of $P_L = 4$ mW and a writing speed of 2.5×10^3 lines per second (by Nanoscribe Photonic Professional GT system). This condition was below the threshold for MPC without plasmonic amplification (Figure S1). After the MPC recording and ethanol rinsing step, the patterned structures were characterized by AFM, and Figure 3c shows the obtained height topography with detailed cross sections presented in Figure 3d. The successful local attachment of the polymer network changed the shape of the individual AuNPs, which became elongated along one axis, forming two apparent lobes stretching to opposite directions into a distance of 50 nm from the AuNP wall (defined as the distance where the height drops to half of its maximum; see Figure 3d). Such a shape can be attributed to the area of the plasmonic hotspot as simulated by FDTD and presented in Figure 2d. For the same AuNP, these simulations predict that the enhanced field intensity reaches a distance of about 50 nm (from the Au wall where the electric field amplitude drops to half of its magnitude; see Figure S2a) that is close to the experimental results. The orientation of the lobes is expected to be aligned with the polarization of the incident NIR fs beam, and irregularities in the shape can be attributed to variations in the plasmonic properties of individual AuNP associated with their polycrystalline nature⁶² and local deviations in shape.⁵⁷

In order to rule out that the polymer features appearing after the irradiation with the fs pulsed laser beam are associated with the effect of burning and to confirm that PE-MPC leads to a polymer network that forms a hydrogel after swelling with water, elastic properties were evaluated by mapping of Young's modulus in air and in water (see Figure 4a,b, respectively).

Both micrographs reveal that around the hard metallic nanoparticles (with Young's modulus >20 GPa), a belt-shaped region with lower stiffness occurs. The evaluation of these data using the elastic contact model according to Hertz with the Sneddon extension for the tip geometry was carried out. It is clearly visible that Young's modulus of the dry polymer network around the AuNPs is around 10 times higher than that for the swollen network immersed in water forming a hydrogel (0–25 GPa for air and 0–2 GPa for water). The values for both Young's moduli in air and water were derived from the histograms of the hydrogel's Young's moduli at random positions (around 30 AuNPs). The maximum of the fitting, representing the most probable value, was then identified as 1.5 ± 0.2 GPa in air and 0.10 ± 0.01 GPa in water. In addition, the degree of swelling of the polymer network was determined by comparing the size of the hydrogel nanostructure (distance between upper and lower) in either air or water ($N = 50$) from AFM images in contact or QI mode (data not shown). The size of the hybrid features in air was 320.3 ± 2.6 nm, while in water, it was slightly larger at 349.2 ± 2.2 nm, which can be attributed to swelling.

It is worth noticing that selective crosslinking occurs only on substrates with λ_{LSPR} of the AuNPs matching the wavelength of the NIR fs laser beam λ_L . This was demonstrated by employing enlarged AuNPs ($D \approx 210$ nm; Figure S4a) with the correspondingly red-shifted LSPR⁵⁷ that became detuned

from λ_L . This leads to a lower field amplitude enhancement factor $|E/E_0|$ at λ_L (as predicted by simulations in Figure S2c) and, therefore, to a weaker plasmonic enhancement effect for triggering the MPC. In this case, a continuous layer of hydrogel is formed around the particles for conditions above the threshold (as seen in Figure S4b), while below it, no polymer is attached over the entire surface.

The second, pNIPAAm-based, polymer network was attached to AuNPs by an NIR fs beam that was polarized along one of the axes of the AuNP arrays. The home-built lithographer setup was used, and this optical system was designed for “point-by-point” writing of desired structures. For this system, a laser power P_L of 15 mW and a dwelling time t_d of 3 s were previously reported to provide the energy dose above the threshold for direct (nonplasmonically enhanced) MPC for the same poly(NIPAAm₉₄-*co*-MAA₅-*co*-BPQAAm₁) terpolymer.⁵⁵ For PE-MPC, the AuNP array with $D = 165 \pm 10$ nm, a height of 50 nm, and a period Λ of 400 nm was exploited, with the LSPR tuned to the used λ_L (see Figure S5). Subsequently, the configuration of the scanning NIR femto-second beam was changed to a decreased power of $P_L = 10$ mW and a shortened dwelling time of $t_d = 1$ s, which is below the threshold for the direct MPC recording but above the threshold for PE-MPC. Figure S6b presents the AFM height topography image of an area with AuNPs bearing the attached pNIPAAm-based network that was dried at room temperature after the rinsing step. Apparently, it does not reveal clear localization of the polymer network around the AuNPs, which we ascribed to its high swelling ratio (>10) as documented by our previous work on direct MPC.⁵⁵ This effect was previously observed in the case of other pNIPAAm-based hydrogel nanostructures attached to a solid substrate and attributed to the strong surface tension of the water–air interface, which deforms the elastic polymer network and leads to a planarization of the soft crosslinked area as it reaches the hydrogel layer during water evaporation.⁶³ However, when the same structure is allowed to swell in water at room temperature and subsequently heated to a higher temperature above the pNIPAAm VPTT before drying, the original crosslinked pattern can be retained (this is schematically shown in Figure S7a). To confirm this, we dried the sample at an elevated temperature of $T = 80$ °C and the results are shown in Figure S7b–d. Specifically, as can be seen from Figure S7c, the hydrogel structure dried at a temperature above its VPTT partially retained the shape, which resembles the plasmonic hotspots (similar to Figure 3c in the case of poly(DMAA₉₆-*co*-AAHAQ₄) copolymer). However, more pronounced smearing of the prepared hydrogel shape occurs for the poly(NIPAAm₉₄-*co*-MAA₅-*co*-BPQAAm₁) hydrogel when compared to poly(DMAA₉₆-*co*-AAHAQ₄), which is attributed to the difference in their swelling ratio (swelling of >10 was estimated for the pNIPAAm-based hydrogel, while only 2.3 was determined for pDMAA-based gel from data in Figure S3).

Polarization-Resolved LSPR Measurements. AFM observation did not clearly reveal the presence of locally attached polymer networks at the AuNP hotspot for the second polymer poly(NIPAAm₉₄-*co*-MAA₅-*co*-BPQAAm₁) with a lower amount of 1% incorporated photocrosslinker, which we attributed to the softer characteristics of the formed hydrogel associated with a lower crosslink density and high swelling ratio. Therefore, we took advantage of the thermoresponsive properties of this pNIPAAm-based hydrogel

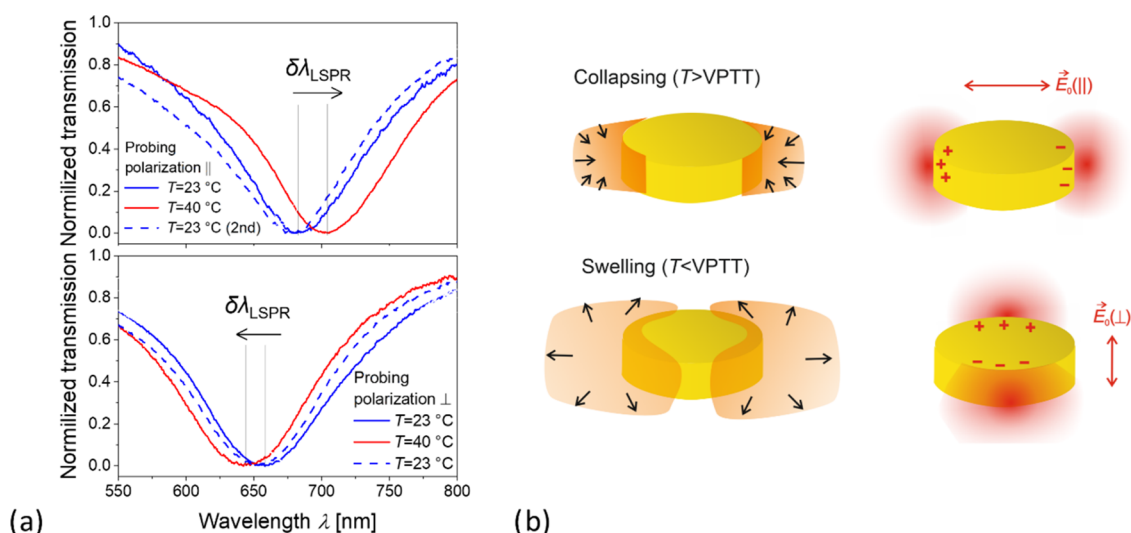


Figure 5. Polarization-resolved white-light transmission measurements of the plasmonically enhanced MPC-written poly(NIPAAm₉₄-co-MAA₅-co-BPQAAm₁) sample: (a) normalized transmission spectra and (b) schematics of the hydrogel swelling and collapsing at the plasmonic hotspots.

and monitored the redistribution of surface mass density around the AuNPs when modulating the temperature above and below the VPTT of pNIPAAm. The LSPR wavelength λ_{LSPR} shifts with changes in the refractive index of the medium surrounding the AuNPs with a magnitude that is proportional to the surface mass density of the polymer materials. As the writing NIR femtosecond beam was made polarized for the PE-MPC, the prepared hydrogel nanostructures are expected to be attached only to the AuNP walls that are perpendicular to the incident electric intensity vector of the writing beam (see the near-field distribution in Figure 2d). In the collapsed state, when the temperature of the structure is above the pNIPAAm VPTT, the polymer network should be compacted at these AuNP sides, while below the VPTT in the swollen state, a delocalization and wrapping over the whole AuNPs is expected owing to its high swelling ratio.

In order to test the presence of the locally attached thermoresponsive pNIPAAm-based hydrogel to AuNPs, transmission LSPR spectra were measured with control over the polarization of the impinging optical beam at varying temperature T . As shown in Figure 5, the polarization of the probing optical beam was noted as “||-pol.” when it is made parallel to, and “⊥-pol.” when perpendicular to the polarization of the writing NIR fs laser beam. The substrate carrying AuNPs with the attached pNIPAAm-based nanostructures was mounted on a transparent temperature-controlled flow cell with water in contact with the surface.

First, measurements were done at room temperature ($T = 23\text{ °C}$), then the temperature was increased to $T = 40\text{ °C}$ above the pNIPAAm VPTT, and finally, it was decreased again to room temperature ($T = 23\text{ °C}$, second). The corresponding measured transmission spectra in Figure 5a show that as the temperature increases above the pNIPAAm VPTT of 32 °C , the LSPR wavelength λ_{LSPR} for ||-pol. (top) red-shifts, while that for ⊥-pol. (bottom) blue-shifts. These shifts are of opposite sign and indicate that the collapse of pNIPAAm leads to asymmetrical redistribution of polymer networks around the AuNPs as an increase in the refractive index on the AuNP walls probed by LSPs with dipole moment parallel to the polarization (||) of the NIR fs laser beam occurs, while on the surface probed by the perpendicular orientation of the

polarization (⊥), the refractive index decreases. This unusual behavior can be explained by assuming that the highly swollen pNIPAAm-based hydrogel nanostructure wraps around the whole AuNP in its swollen state. When increasing the temperature T above the LCST, the hydrogel compacts at the AuNP walls where it was attached by the plasmonically enhanced intensity of the NIR fs laser beam (Figure 5b). This effect is accompanied by an increased surface mass density and a higher refractive index of the hydrogel on walls perpendicular to the polarization (||) of the writing beam. On the surface of walls parallel to the fs NIR beam polarization (⊥) where the polymer network is not attached, it therefore retracts toward the plasmonic hotspots and is replaced by water with a lower refractive index of $n_{\text{H}_2\text{O}} = 1.33$. Importantly, these transitions are reversible, and as the structure is cooled back to $T = 23\text{ °C}$, which is below the VPTT, the LSPR wavelengths shift to their original position. The magnitude of the LSPR shift for the || probing polarization is $\Delta\lambda_{\text{LSPR}} = 22\text{ nm}$ (which is close to that measured for a pNIPAAm film that covers the whole area of similar AuNP arrays⁶⁴), and it corresponds to the refractive index change of $\Delta n_{\text{h}} = 0.11$ with a respective swelling ratio of about 7.5. The measured LSPR shift for the orthogonal polarization ⊥ is of $\Delta\lambda_{\text{LSPR}} = -14\text{ nm}$ and corresponds to the refractive index change of $\Delta n_{\text{h}} = -0.07$. This change would translate to a refractive index of the swollen hydrogel of $n_{\text{h}} = 1.40$, which corresponds to a lower swelling ratio and indicates that local gradients of the swelling process occurring in a quasi-three-dimensional manner play a significant role. Let us also note that the water surrounding the structure also changes its refractive index with temperature with a thermo-optical coefficient of $dn_{\text{H}_2\text{O}}/dT = -1.2 \times 10^{-4}\text{ RIU/K}$, but this effect can be neglected as it is associated with a much smaller decrease in the resonant wavelength of -0.4 nm for the temperature change of 17 K .

CONCLUSIONS

Selective attachment of polymer networks forming a hydrogel at the plasmonic hotspot regions of metallic nanostructures is achieved. The obtained hybrid polymer–metallic nanostructure was prepared with nanoscale spatial precision by plasmon-enhanced multiphoton crosslinking of the presynthesized

polymer chains conjugated with photoactive crosslinkers. With the use of optical configurations already established for a two-photon lithography relying on optically triggered polymerization, the reported alternative approach based on polymer crosslinking⁵⁵ provides a facile means for local attachment of the functional hydrogel materials at the areas, where the electromagnetic field is strongly confined. This functionality is highly relevant in the fields of optical bioanalytical technologies and optical spectroscopy that take advantage of the plasmonically enhanced output optical signal. The prepared polymer network can be converted into a hydrogel serving as a three-dimensional large binding capacity matrix when postmodified with biorecognition elements.^{65,66} In plasmonic bioanalytical tools, such a binding matrix is designed to efficiently capture target analyte molecules from an analyzed liquid sample contacted with the sensor surface. In combination with the thermoresponsive properties, the optical readout sensitivity can be improved by using a hydrogel matrix that in the swollen state binds the target analyte inside its open network structure followed by its compacting at the plasmonic hotspot via a thermally induced network collapse performed prior to the optical readout. This approach provides dual amplification means, and it was already investigated with a thin pNIPAAm-based hydrogel binding matrix layer collapsing in the direction perpendicular to the surface in conjunction with the optical probing by surface plasmons propagating along the thin metallic film.⁶⁷ When using the tighter confined and stronger amplified LSP field generated on metallic nanoparticles, the performance of such a sensor can simultaneously capitalize on stronger optical enhancement and on compacting the captured analyte species at narrower and sparser distributed plasmonic hotspots via a collapse in both perpendicular and parallel directions. The proposed approach may pave the way to such a new class of hybrid plasmonic structures tailored for the optical biosensor and spectroscopy applications with improved accuracy.⁶⁶

■ ASSOCIATED CONTENT

Data Availability Statement

The data that support this study are openly available at [10.17605/OSF.IO/V52GB](https://doi.org/10.17605/OSF.IO/V52GB).

SI Supporting Information

The Supporting Information is available free of charge at <https://pubs.acs.org/doi/10.1021/acs.jpcc.4c05936>.

Additional experimental details and results of electromagnetic numerical simulations, AFM topography of control structures, and used thin film characteristics (PDF)

■ AUTHOR INFORMATION

Corresponding Authors

Yevhenii M. Morozov – Center for Health & Bioresources, AIT-Austrian Institute of Technology, 1210 Vienna, Austria; orcid.org/0000-0001-9689-8641;

Email: yevhenii.morozov@ait.ac.at

Jakub Dostalek – FZU-Institute of Physics, Czech Academy of Sciences, 182 21 Prague, Czech Republic; LiST-Life Sciences Technology, Danube Private University, 2700 Wiener Neustadt, Austria; orcid.org/0000-0002-0431-2170;

Email: dostalek@fzu.cz

Authors

Nestor Gisbert Quilis – Biosensor Technologies, AIT-Austrian

Institute of Technology, 3430 Tulln an der Donau, Austria

Stefan Fossati – FZU-Institute of Physics, Czech Academy of Sciences, 182 21 Prague, Czech Republic

Laura De Laporte – DWI-Leibniz Institute for Interactive Materials, D-52074 Aachen, Germany; Institute for Technical and Macromolecular Chemistry, RWTH Aachen University, D-52074 Aachen, Germany; Institute of Applied Medical Engineering, Department of Advanced Materials for Biomedicine, RWTH Aachen University, D-52074 Aachen, Germany; orcid.org/0000-0002-9438-0977

Claudia Gusenbauer – Institute of Wood Technology and Renewable Materials, University of Natural Resources and Life Sciences, 3430 Tulln an der Donau, Austria;

orcid.org/0000-0003-3520-3732

Andreas Weber – Institute of Biophysics, University of Natural Resources and Life Sciences, 1190 Vienna, Austria

Jose Luis Toca-Herrera – Institute of Biophysics, University of Natural Resources and Life Sciences, 1190 Vienna, Austria

Fiona Wiesner – Macromolecular Chemistry, Department of Chemistry and Biology, University of Siegen, 57074 Siegen, Germany

Ulrich Jonas – Macromolecular Chemistry, Department of Chemistry and Biology, University of Siegen, 57074 Siegen, Germany; orcid.org/0000-0002-2161-4541

Complete contact information is available at:

<https://pubs.acs.org/10.1021/acs.jpcc.4c05936>

Author Contributions

The manuscript was written through the contributions of all authors. All authors have approved the final version of the manuscript.

Notes

The authors declare no competing financial interest.

■ ACKNOWLEDGMENTS

Y.M. acknowledges support from the Austrian Science Fund (FWF) through the Lise Meitner Programme (M 2925). J.D. and S.F. are grateful for the support from Operational Programme Johannes Amos Comenius financed by European Structural and Investment Funds and the Czech Ministry of Education, Youth and Sports (Project No. SENDISO - CZ.02.01.01/00/22_008/0004596), the Czech Science Fund through the project APLOMA (22-30456J), and from the European Commission via the project VerSiLib (101046217). Y.M. expresses gratitude to Giorgio Mutinati (Austrian Institute of Technology) for his assistance with the IonSys 500 instrument. Open access publishing facilitated by Fyzikalni ustav Akademie ved Ceske republiky, as part of the ACS - CzechELib agreement.

■ ABBREVIATIONS

AAHAQ, acylamido-3-hydroxyanthraquinone; AFM, atomic force microscopy; AuNP, gold nanoparticle; BPdiS, 3,3'-disulfanediybis(*N*-(4-benzoylbenzyl)propanamide); BPQAAM, quaternary ammonium cation *N*-(4-benzoylphenyl)acrylamide; DMAA, dimethylacrylamide; DMSO, dimethyl sulfoxide; FDTD, finite-difference time-domain; LCST, local critical solution temperature; LSP, localized surface plasmon; LSPR, localized surface plasmon resonance; MAA, methacrylic acid; MPC, multiphoton cross-

linking; NIPAAm, *N*-isopropylacrylamide; NIR, near-infrared; NP, nanoparticle; PE-MPC, plasmon-enhanced multiphoton crosslinking; QI, AFM quantitative imaging mode; VPTT, volume phase transition temperature

REFERENCES

- (1) Gramotnev, D. K.; Bozhevolnyi, S. I. Plasmonics beyond the diffraction limit. *Nat. Photonics* **2010**, *4*, 83–91.
- (2) Homola, J.; Yee, S. S.; Gauglitz, G. Surface plasmon resonance sensors: Review. *Sens. Actuators, B* **1999**, *54* (1–2), 3–15.
- (3) Christopher, P.; Xin, H.; Linic, S. Visible-light-enhanced catalytic oxidation reactions on plasmonic silver nanostructures. *Nat. Chem.* **2011**, *3*, 467–472.
- (4) Wang, X. A.; Kong, X. Review of recent progress of plasmonic materials and nano-structures for surface-enhanced Raman scattering. *Materials* **2015**, *8* (6), 3024–3052.
- (5) Rosman, C.; Prasad, J.; Neiser, A.; Henkel, A.; Edgar, J.; Sönnichsen, C. Multiplexed plasmon sensor for rapid label-free analyte detection. *Nano Lett.* **2013**, *13* (7), 3243–3247.
- (6) Brasselet, S. Polarization-resolved microscopy in the life sciences. *Opt. Photonics News* **2019**, *30* (4), 34–41.
- (7) Zuo, T.; Goldwyn, H. J.; Isaacoff, B. P.; Masiello, D. J.; Biteen, J. S. Rotation of single-molecule emission polarization by plasmonic nanorods. *J. Phys. Chem. Lett.* **2019**, *10* (17), 5047–5054.
- (8) Zijlstra, P.; Paulo, P. M. R.; Orrit, M. Optical detection of single non-absorbing molecules using the surface plasmon resonance. *Nat. Nanotechnol.* **2012**, *7*, 379–382.
- (9) Liang, L.; Zheng, P.; Jia, S.; Ray, K.; Chen, Y.; Barman, I. Plasmonic nanodiamonds. *Nano Lett.* **2023**, *23* (12), 5746–5754.
- (10) Taylor, A. B.; Zijlstra, P. Single-molecule plasmon sensing: Current status and future prospects. *ACS Sens.* **2017**, *2* (8), 1103–1122.
- (11) Zhang, X.; Li, X.; Reish, M. E.; Zhang, D.; Su, N. Q.; Gutiérrez, Y.; Moreno, F.; Yang, W.; Everitt, H. O.; Liu, J. Plasmon-enhanced catalysis: Distinguishing thermal and nonthermal effects. *Nano Lett.* **2018**, *18* (3), 1714–1723.
- (12) Ezendam, S.; Gargiulo, J.; Sousa-Castillo, A.; Lee, J. B.; Nam, Y. S.; Maier, S. A.; Cortés, E. Spatial distributions of single-molecule reactivity in plasmonic catalysis. *ACS Nano* **2024**, *18* (1), 451–460.
- (13) Xia, Y.; Halas, N. J. Shape-controlled synthesis and surface plasmonic properties of metallic nanostructures. *MRS Bull.* **2005**, *30* (5), 338–348.
- (14) Moskovits, M. Spot the hotspot. *Nature* **2011**, *469* (7330), 307–309.
- (15) Feuz, L.; Jonsson, M. P.; Höök, F. Material-selective surface chemistry for nanoplasmonic sensors: Optimizing sensitivity and controlling binding to local hot spots. *Nano Lett.* **2012**, *12*, 873–879.
- (16) Feuz, L.; Jönsson, P.; Jonsson, M. P.; Höök, F. Improving the limit of detection of nanoscale sensors by directed binding to high-sensitivity areas. *ACS Nano* **2010**, *4* (4), 2167–2177.
- (17) Beeram, S. R.; Zamborini, F. P. Selective attachment of antibodies to the edges of gold nanostructures for enhanced localized surface plasmon resonance biosensing. *J. Am. Chem. Soc.* **2009**, *131* (33), 11689–11691.
- (18) Zhang, N.; Liu, Y. J.; Yang, J.; Su, X.; Deng, J.; Chum, C. C.; Hong, M.; Teng, J. High sensitivity molecule detection by plasmonic nanoantennas with selective binding at electromagnetic hotspots. *Nanoscale* **2014**, *6* (3), 1416–1422.
- (19) Piliarik, M.; Kvasnička, P.; Galler, N.; Krenn, J. R.; Homola, J. Local refractive index sensitivity of plasmonic nanoparticles. *Opt. Express* **2011**, *19* (10), 9213–9220.
- (20) Oliverio, M.; Perotto, S.; Messina, G. C.; Lovato, L.; de Angelis, F. Chemical functionalization of plasmonic surface biosensors: A tutorial review on issues, strategies, and costs. *ACS Appl. Mater. Interfaces.* **2017**, *9* (35), 29394–29411.
- (21) Barik, A.; Otto, L. M.; Yoo, D.; Jose, J.; Johnson, T. W.; Oh, S.-H. Dielectrophoresis-enhanced plasmonic sensing with gold nanohole arrays. *Nano Lett.* **2014**, *14* (4), 2006–2012.
- (22) Gargiulo, J.; Berté, R.; Li, Y.; Maier, S. A.; Cortés, E. From optical to chemical hot spots in plasmonics. *Acc. Chem. Res.* **2019**, *52* (9), 2525–2535.
- (23) Gruber, C.; Hirzer, A.; Schmidt, V.; Trügler, A.; Hohenester, U.; Ditzbacher, H.; Hohenau, A.; Krenn, J. R. Imaging nanowire plasmon modes with two-photon polymerization. *Appl. Phys. Lett.* **2015**, *106* (8), No. 081101.
- (24) Galloway, C. M.; Kreuzer, M. P.; Ćimović, S. S.; Volpe, G.; Correia, M.; Petersen, S. B.; Neves-Petersen, M. T.; Quidant, R. Plasmon-assisted delivery of single nano-objects in an optical hot spot. *Nano Lett.* **2013**, *13* (9), 4299–4304.
- (25) Magill, B. A.; Guo, X.; Peck, C. L.; Reyes, R. L.; See, E. M.; Santos, W. L.; Robinson, H. D. Multi-photon patterning of photoactive *o*-nitrobenzyl ligands bound to gold surfaces. *Photochem. Photobiol. Sci.* **2019**, *18* (1), 30–44.
- (26) Pin, C.; Ishida, S.; Takahashi, G.; Sudo, K.; Fukaminato, T.; Sasaki, K. Trapping and deposition of dye–molecule nanoparticles in the nanogap of a plasmonic antenna. *ACS Omega* **2018**, *3* (5), 4878–4883.
- (27) Rajeeva, B. B.; Hernandez, D. S.; Wang, M.; Perillo, E.; Lin, V.; Scarabelli, L.; Pingali, V.; Liz-Marzán, L. M.; Dunn, V.; Shear, V.; Zheng, Y. Regioselective localization and tracking of biomolecules on single gold nanoparticles. *Adv. Sci.* **2015**, *2* (11), No. 1500232.
- (28) Sundaramurthy, A.; James Schuck, P.; Conley, N. R.; Fromm, D. P.; Kino, G. S.; Moerner, W. E. Toward nanometer-scale optical photolithography: Utilizing the near-field of bowtie optical nanoantennas. *Nano Lett.* **2006**, *6* (3), 355–360.
- (29) Ueno, K.; Juodkazis, S.; Shibuya, T.; Yokota, Y.; Mizeikis, V.; Sasaki, K.; Misawa, H. Nanoparticle plasmon-assisted two-photon polymerization induced by incoherent excitation source. *J. Am. Chem. Soc.* **2008**, *130* (22), 6928–6929.
- (30) Ueno, K.; Juodkazis, S.; Shibuya, T.; Mizeikis, V.; Yokota, Y.; Misawa, H. Nanoparticle-enhanced photopolymerization. *J. Phys. Chem. C* **2009**, *113* (27), 11720–11724.
- (31) Nah, S.; Li, L.; Liu, R.; Hao, J.; Lee, S. B.; Fourkas, J. T. Metal-enhanced multiphoton absorption polymerization with gold nanowires. *J. Phys. Chem. C* **2010**, *114* (17), 7774–7779.
- (32) Yokoyama, T.; Masuhara, A.; Onodera, T.; Kasai, H.; Oikawa, H. Plasmon-enhanced photopolymerization of SU-8 on rough gold surfaces. *J. Phys. Chem. C* **2010**, *114* (46), 19596–19599.
- (33) Kameche, F.; Heni, W.; Telitel, S.; Ge, D.; Vidal, L.; Dumur, F.; Gignes, D.; Lalevée, J.; Marguet, S.; Douillard, L.; Fiorini-Debuisschert, C.; Bachelot, R.; Soppera, O. Plasmon-triggered living photopolymerization for elaboration of hybrid polymer/metal nanoparticles. *Mater. Today* **2020**, *40*, 38–47.
- (34) Kameche, F.; Heni, W.; Telitel, S.; Ge, D.; Vidal, L.; Marguet, S.; Douillard, L.; Fiorini-Debuisschert, C.; Bachelot, R.; Soppera, O. Probing plasmon-induced chemical mechanisms by free-radical nanophotopolymerization. *J. Phys. Chem. C* **2021**, *125* (16), 8719–8731.
- (35) Khitous, A.; Molinaro, C.; Gree, S.; Haupt, K.; Soppera, O. Plasmon-induced photopolymerization of molecularly imprinted polymers for nanosensor applications. *Adv. Mater. Interfaces* **2023**, *10* (7), No. 2201651.
- (36) Lee, J.; Joshi, P. B.; Wilson, A. J.; Kim, Y. Plasmon-driven near-field photopolymerization in a gold nanoparticle colloid. *J. Phys. Chem. C* **2023**, *127* (17), 8096–8103.
- (37) Khitous, A.; Molinaro, C.; Abdallah, S.; Chen, M.; Marguet, S.; Laurent, G.; Vidal, L.; Malval, J.-P.; Fiorini-Debuisschert, C.; Adam, P.-M.; Douillard, L.; Bachelot, R.; Soppera, O. Spatial distribution of the photopolymerization induced by localized surface plasmons: Impact of the morphology of the Au nanoparticles. *J. Phys. Chem. C* **2024**, *128* (31), 13097–13107.
- (38) Maruo, S.; Nakamura, O.; Kawata, S. Three-dimensional microfabrication with two-photon-absorbed photopolymerization. *Opt. Lett.* **1997**, *22* (2), 132–134.
- (39) Sun, H.-B.; Kawata, S. Two-photon laser precision microfabrication and its applications to micro-nano devices and systems. *J. Lightwave Technol.* **2003**, *21* (3), 624–633.

- (40) Farsari, M.; Chichkov, B. Materials processing: Two-photon fabrication. *Nat. Photonics* **2009**, *3*, 450–452.
- (41) Gissibl, T.; Thiele, S.; Herkommer, A.; Giessen, H. Two-photon direct laser writing of ultracompact multi-lens objectives. *Nat. Photonics* **2016**, *10* (8), S54–S60.
- (42) Florian, C.; Piazza, S.; Diaspro, A.; Serra, P.; Duocastella, M. Direct laser printing of tailored polymeric microlenses. *ACS Appl. Mater. Interfaces* **2016**, *8* (27), 17028–17032.
- (43) Gissibl, T.; Thiele, S.; Herkommer, A.; Giessen, H. Sub-micrometre accurate free-form optics by three-dimensional printing on single-mode fibres. *Nat. Commun.* **2016**, *7*, No. 11763.
- (44) Avci, E.; Grammatikopoulou, M.; Yang, G. Z. Laser-printing and 3D optical-control of untethered microrobots. *Adv. Opt. Mater.* **2017**, *5* (19), No. 1700031.
- (45) Zeng, H.; Martella, D.; Wasylczyk, P.; Cerretti, G.; Lavocat, J. C. G.; Ho, C. H.; Parmeggiani, C.; Wiersma, D. S. High-resolution 3D direct laser writing for liquid-crystalline elastomer microstructures. *Adv. Mater.* **2014**, *26* (15), 2319–2322.
- (46) Selimis, A.; Mironov, V.; Farsari, M. Direct laser writing: Principles and materials for scaffold 3D printing. *Microelectron. Eng.* **2015**, *132*, 83–89.
- (47) Accardo, A.; Blatché, M. C.; Courson, R.; Loubinoux, I.; Thibault, C.; Malaquin, L.; Vieu, C. Multiphoton direct laser writing and 3D imaging of polymeric freestanding architectures for cell colonization. *Small* **2017**, *13* (27), No. 1700621.
- (48) Hippler, M.; Lemma, E. D.; Bertels, S.; Blasco, E.; Barner-Kowollik, C.; Wegener, M.; Bastmeyer, M. 3D scaffolds to study basic cell biology. *Adv. Mater.* **2019**, *31* (26), No. 1808110.
- (49) Song, J.; Michas, C.; Chen, C. S.; White, A. E.; Grinstaff, M. W. From simple to architecturally complex hydrogel scaffolds for cell and tissue engineering applications: Opportunities presented by two-photon polymerization. *Adv. Healthcare Mater.* **2019**, *9* (1), No. 1901217.
- (50) Jing, X.; Fu, H.; Yu, B.; Sun, M.; Wang, L. Two-photon polymerization for 3D biomedical scaffolds: Overview and updates. *Front. Bioeng. Biotechnol.* **2022**, *10*, No. 994355.
- (51) Mckee, S.; Lutey, A.; Sciancalepore, C.; Poli, F.; Selleri, S.; Cucinotta, A. Microfabrication of polymer microneedle arrays using two-photon polymerization. *J. Photochem. Photobiol., B* **2022**, *229*, No. 112424.
- (52) Zhou, X.; Hou, Y.; Lin, J. A review on the processing accuracy of two-photon polymerization. *AIP Adv.* **2015**, *5* (3), No. 030701.
- (53) Niesler, F.; Hermatschweiler, M. Two-photon polymerization—A versatile microfabrication tool: From maskless lithography to 3D printing. *Laser Tech. J.* **2015**, *12* (3), 44–47.
- (54) Schwärzle, D.; Hou, X.; Prucker, O.; Rühle, J. Polymer microstructures through two-photon crosslinking. *Adv. Mater.* **2017**, *29* (39), No. 1703469.
- (55) Morozov, Y. M.; Wiesner née Diehl, F.; Grün, J. J.; Pertiller, M.; Fossati, S.; Schmidt, K.; Quilis, N. G.; Gusenbauer, C.; Zbiral, B.; Toca-Herrera, J. L.; Klees, S.; Thiagarajan, C. R. V.; Jonas, U.; Dostalek, J. Microstructuring of thermoresponsive biofunctional hydrogels by multiphoton photocrosslinking. *Adv. Funct. Mater.* **2024**, *34* (26), No. 2315578.
- (56) Sergelen, K.; Petri, C.; Jonas, U.; Dostalek, J. Free-standing hydrogel-particle composite membrane with dynamically controlled permeability. *Biointerphases* **2017**, *12* (5), No. 051002.
- (57) Gisbert Quilis, N.; Lequeux, M.; Venugopalan, P.; Khan, I.; Knoll, W.; Boujday, S.; de la Chapelle, M. L.; Dostalek, J. Tunable laser interference lithography preparation of plasmonic nanoparticle arrays tailored for SERS. *Nanoscale* **2018**, *10* (21), 10268–10276.
- (58) Bunea, A.-I.; del Castillo Iniesta, N.; Droumpali, A.; Wetzels, A. E.; Engay, E.; Taboryski, R. Micro 3D printing by two-photon polymerization: Configurations and parameters for the Nanoscribe system. *Micro* **2021**, *1* (2), 164–180.
- (59) Morozov, Y. M.; Quilis, N. G.; Diehl, F.; Klees, S.; Grün, J.; Jonas, U.; Dostalek, J. One- and two-photon crosslinked polymer hydrogel microstructures for optical spectroscopy and biosensing applications. *Proc. SPIE* **2022**, *12145*, No. 1214502.
- (60) Johnson, P. B.; Christy, R. W. Optical constants of the noble metals. *Phys. Rev. B* **1972**, *6* (12), 4370.
- (61) Johnson, P. B.; Christy, R. W. Optical constants of transition metals: Ti, V, Cr, Mn, Fe, Co, Ni, and Pd. *Phys. Rev. B* **1974**, *9* (12), 5056.
- (62) Kejík, L.; Horák, M.; Šikola, T.; Křápek, V. Structural and optical properties of monocrystalline and polycrystalline gold plasmonic nanorods. *Opt. Express* **2020**, *28* (23), 34960–34972.
- (63) Sharma, N.; Petri, C.; Jonas, U.; Dostalek, J. Reversibly tunable plasmonic bandgap by responsive hydrogel grating. *Opt. Express* **2016**, *24* (3), 2457–2465.
- (64) Auer, S. K.; Fossati, S.; Morozov, Y.; Mor, D. C.; Jonas, U.; Dostalek, J. Rapid actuation of thermo-responsive polymer networks: Investigation of the transition kinetics. *J. Phys. Chem. B* **2022**, *126* (16), 3170–3179.
- (65) Mateescu, A.; Wang, Y.; Dostalek, J.; Jonas, U. Thin hydrogel films for optical biosensor applications. *Membranes* **2012**, *2* (1), 40–69.
- (66) Diehl, F.; Hageneder, S.; Fossati, S.; Auer, S. K.; Dostalek, J.; Jonas, U. Plasmonic nanomaterials with responsive polymer hydrogels for sensing and actuation. *Chem. Soc. Rev.* **2022**, *51* (10), 3926–3963.
- (67) Hageneder, S.; Jungbluth, V.; Soldo, R.; Petri, C.; Pertiller, M.; Kreivi, M.; Weinhäusel, A.; Jonas, U.; Dostalek, J. Responsive hydrogel binding matrix for dual signal amplification in fluorescence affinity biosensors and peptide microarrays. *ACS Appl. Mater. Interfaces* **2021**, *13* (23), 27645–27655.